# *Expansivity and compressibility of strontium fluorapatite and barium fluorapatite determined by in situ X-ray diffraction at high-T/P conditions: significance of the M-site cations*

**Qiang He, Xi Liu, Baosheng Li, Liwei Deng, Zhiqiang Chen, Xiaoyang Liu & Hejing Wang**

**Physics and Chemistry of Minerals**

ISSN 0342-1791

Phys Chem Minerals
DOI 10.1007/s00269-013-0576-6

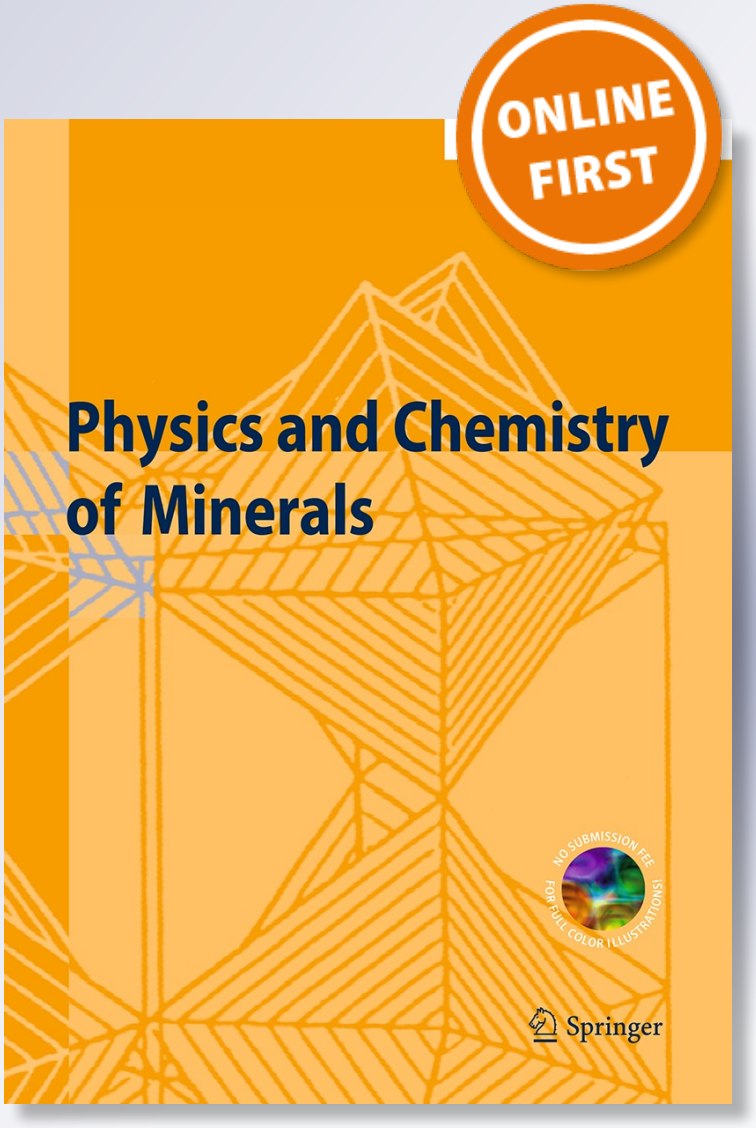


Springer

Phys Chem Minerals
DOI 10.1007/s00269-013-0576-6

ORIGINAL PAPER

# Expansivity and compressibility of strontium fluorapatite and barium fluorapatite determined by in situ X-ray diffraction at high-*T*/*P* conditions: significance of the M-site cations

**Qiang He · Xi Liu · Baosheng Li · Liwei Deng · Zhiqiang Chen · Xiaoyang Liu · Hejing Wang**

Received: 11 October 2012 / Accepted: 3 February 2013


**Abstract** Strontium fluorapatite (SrF-Ap) and barium fluorapatite (BaF-Ap) were synthesized by using a piston-cylinder apparatus at 1.0 GPa and 800 °C. Their thermal expansivity and compressibility were subsequently investigated by using in situ high-*T* powder X-ray diffraction method (up to 1,000 °C at ambient *P*) and by using a diamond-anvil cell coupled with synchrotron X-ray radiation (up to about 5 GPa at room *T*), respectively. The derived thermal expansion coefficients and bulk moduli were combined with the literature data for calcium fluorapatite (CaF-Ap) and lead fluorapatite (PbF-Ap) to constrain the influence of the M-site cations on the elasticity of the fluorapatites (MF-Ap). The results show that both the size of the M cations and their polarizability affect the thermal expansion coefficients of the MF-Ap. For the axial and volumetric bulk moduli, the size of the M cations plays a dominant role, with some crystallographic features of the MF-Ap being potentially important as well.

**Keywords** Barium fluorapatite · Compressibility · Expansivity · M-site cations · Strontium fluorapatite · X-ray diffraction

Q. He · X. Liu (✉) · H. Wang
Key Laboratory of Orogenic Belts and Crustal Evolution, MOE, Peking University, Beijing 100871, People's Republic of China
e-mail: xi.liu@pku.edu.cn

Q. He · X. Liu · H. Wang
School of Earth and Space Sciences, Peking University, Beijing 100871, People's Republic of China

B. Li · Z. Chen
Mineral Physics Institute, State University of New York, Stony Brook, New York 11794, USA

L. Deng
Geophysical Laboratory, Carnegie Institution of Washington, 5251 Broad Branch Road, NW, Washington, DC 20015, USA

X. Liu
State Key Laboratory of Inorganic Synthesis and Preparative Chemistry, College of Chemistry, Jilin University, Changchun 130012, China

## Introduction

There is no doubt that apatite is an accessory phase in most geological settings. Yet, its crystal chemical characteristics, such as extensive anion/cation substitution and volatile content (Pan and Fleet 2002, and references therein), lead to numerous useful applications in Earth sciences, especially in dating and petrogenesis (e.g., Li et al. 2000; Filiberto and Treiman 2009). Geologically, the most important species of apatite are fluorapatite sensu stricto, hydroxylapatite and chlorapatite ($Ca_{10}(PO_4)_6X_2$ with X = F, OH or Cl). High-*P* experiments have demonstrated that these apatites are stable up to the *P*–*T* conditions of the upper mantle of the Earth (about 12 GPa; Murayama et al. 1986), suggesting a good understanding of their equations of state at high-*P*/*T* conditions is important. Direct compression experiments have been conducted to investigate their compressibility (Brunet et al. 1999; Comodi et al. 2001; Matsukage et al. 2004), and in situ high-*T* X-ray diffraction experiments have been carried out to constrain their thermal expansivity (Fischer et al. 1983; Brunet et al. 1999). The knowledge acquired from these experiments has substantially enhanced our understanding of the effects of the volatile components at the X sites on the elasticity of the apatites.

The general chemical formula of apatite can be written as $M_{10}(BO_4)_6X_2$, with the M sites primarily occupied by

Published online: 17 February 2013

large cations such as $Na^{+}$, $Ca^{2+}$, $Mn^{2+}$, $Cd^{2+}$, $Ba^{2+}$, $Sr^{2+}$, $Pb^{2+}$, $Al^{3+}$ and rare earth elements ($REE^{3+}$); the B sites commonly by $P^{5+}$, $V^{5+}$, $As^{5+}$, $S^{6+}$ and $Si^{4+}$; and the X sites by halides, hydrogen-carbonate cation (Fleet and Liu 2007), oxy-anions, vacancies and small neutral molecules such as $H_2O$ (Pan and Fleet 2002, and references therein). Apparently, the geologically significant fluorapatite sensu stricto (CaF-Ap), hydroxylapatite (CaOH-Ap) and chlorapatite (CaCl-Ap) have their compositional variation at the X sites. The compositional variations at the M sites and B sites also lead to the formation of a large number of apatites (Kreidler and Hummel 1970; Pan and Fleet 2002), some of which bear important geological applications as well (Edgar 1989; Krenn and Finger 2004; Moëlo et al. 2008; Solovova et al. 2009; Zhang et al. 2011). With the experimental investigations of He et al. (2011, 2012), we have had some knowledge about the effect of the cation substitution at the B sites on the elasticity of the apatites. However, the effect of the cation substitution at the M sites on the elasticity of the apatites remains largely unexplored.

As demonstrated by some synthesizing experiments, $Sr^{2+}$ and $Ba^{2+}$, by replacing the $Ca^{2+}$ cations at the M sites, can easily enter the apatite structure (Kreidler and Hummel 1970; Mathew et al. 1979; Khattech and Jemal 1997; Aissa et al. 2004; Sghir et al. 2009). So far, natural Sr-rich apatite and Ba-rich apatite have been found in a large number of locations with different geological settings, such as the leucitite-ijolite xenoliths in the Dangzishan mountain in northeastern China (Zhang et al. 2011, and references therein). In order to understand the phase relations which these apatites involve in, it is desirable to constrain their volume dependence on pressure and temperature.

In this study, we synthesized the strontium fluorapatite [SrF-Ap; $Sr_{10}(PO_4)_6F_2$] and barium fluorapatite [BaF-Ap; $Ba_{10}(PO_4)_6F_2$] with a piston-cylinder apparatus and determined their thermal elasticity and compressibility by using in situ X-ray diffraction method at high-*T*/*P* conditions. Combining our new data with the literature data about the calcium fluorapatite [CaF-Ap; $Ca_{10}(PO_4)_6F_2$] and lead fluorapatite [PbF-Ap; $Pb_{10}(PO_4)_6F_2$], we further explored the effect of the M-site cations on these physical properties of fluorapatites [MF-Ap; $M_{10}(PO_4)_6F_2$].

## Experimental methods

We conducted the synthesizing experiments with a piston-cylinder apparatus (Depths of the Earth Company Quickpress), newly installed at the High-Pressure Laboratory of Peking University. Following Mathew et al. (1979), we prepared the starting materials using reagent grade chemicals such as SrO or BaO, $P_2O_5$ and $SrF_2$ or $BaF_2$. Before mixed together in the required proportions, all these chemicals but $P_2O_5$ were dried in an oven at 110 °C and 1 atm for about 2 days. The $P_2O_5$ powder was not pretreated by any means due to its toxicity and easy evaporation at elevated temperatures. Rather, we added into the starting materials $P_2O_5$ in amounts more than required by the ideal chemical formulas of SrF-Ap and BaF-Ap (5 wt%) to take account of its possible moisture content absorbed from air, right as we did before (He et al. 2011). These mixtures were thoroughly homogenized under alcohol in an agate mortar, let drying up in open air and then stored in an oven at 110 °C for later high-*P* synthesizing experiments. The setup of the Quickpress used in this study was generally identical to what we used in our previous investigations (Fleet and Liu 2007; Liu et al. 2011a), and the experimental techniques were fully reported in Liu and Fleet (2009). The materials were encapsulated into Pt tube (OD = 5, ID = 4.6 and L = 10 mm) which was arc-welded at both ends. The synthesizing conditions were 1.0 GPa, 800 °C and about 24 h. For either SrF-Ap or BaF-Ap, three high-*P* synthesizing experiments were conducted in order to generate enough material for later investigation.

We processed some splits of the synthetic products from the high-*P* synthesizing experiments and examined them with an optical microscope, a confocal micro-Raman system (Renishaw system RM-1,000), a scanning electron microscope (Quanta 200 FEG) and an electron microprobe (JEOL JXA-8,100) at the School of Earth and Space Sciences, Peking University. The left samples were finely ground and checked at ambient condition with a powder X-ray diffractometer (X'Pert Pro MPD system; Cu-$K\alpha$1 X-ray radiation).

We ran the in situ high-*T* powder X-ray diffraction experiments (1 atm) with the X'Pert Pro MPD system, which had an attached Anton Paar HTK-1,200 N oven. The temperature of the oven was controlled by using a Eurotherm temperature controller (Eurotherm 2,604; type S thermocouple checked against the melting point of NaCl). With this heating system, we were able to reach a maximum temperature of 1,200 °C with an accuracy of ± 2 °C (Hu et al. 2011). Other details of the X'Pert Pro MPD diffractometer system were a Cu target, an operation voltage of 40 kV and an operation current of 40 mA. The experimental procedures were as follows: With the completion in collecting the X-ray diffraction data at one temperature, the experimental temperature was raised to another set point by 10 °C/min and then kept constant for 5 min to allow the material to relax before collection of the powder diffraction pattern. We collected the X-ray data from 10 to 80° ($2\theta$), with a scanning step width of 0.017° and a counting time of 10 s for each scanning step. The alignment of the X-ray diffractometer system was checked

by using a standard of silicon crystalline powder at ambient temperature only. Due to the thermal expansion of the furnace and sample holder components, the sample position should have changed slightly at elevated temperatures. Following the data-processing procedure verified in our previous investigations (Hu et al. 2011; He et al. 2011), we were able to correct the influence of this small sample displacement: a full powder X-ray pattern refinement with the MDI's program Jade 5.0 (Material Data, Inc.) led to highly-accurate unit-cell parameters indeed.

With a symmetrical diamond-anvil cell, we carried out our high-*P* powder X-ray diffraction experiments (ambient *T*) at the beamline X17C, National Synchrotron Light Source, Brookhaven National Laboratory. The gaskets used in our experiments were T301 stainless steel plates (initial thickness = 250 μm). The central area of the plates was pre-indented (thickness = 40 μm), and a small hole (diameter = 160 μm) was electrically eroded. The fluorapatite powder and a tiny ruby ball were loaded into the hole in the gasket. The pressure medium was a 4:1

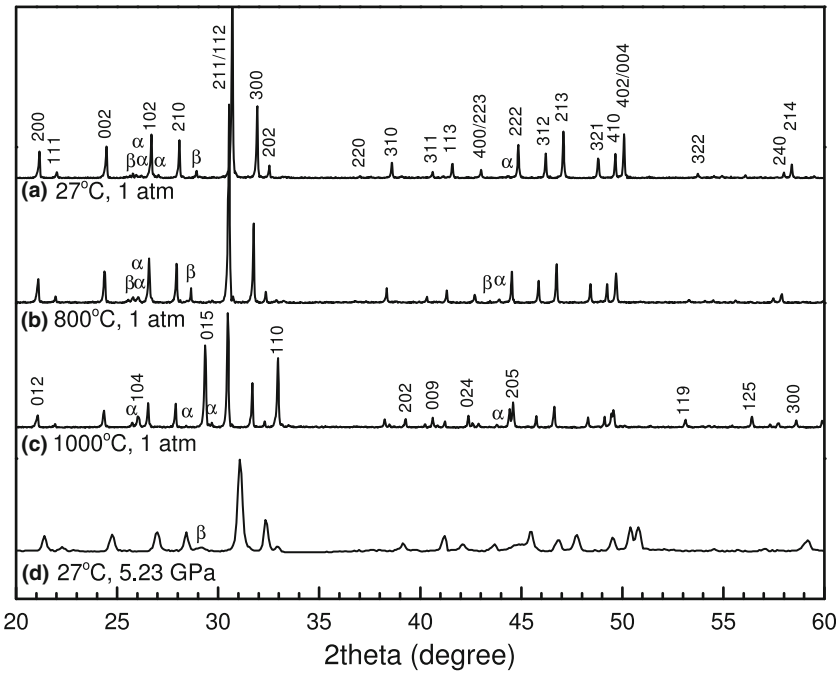


**Fig. 1** Typical XRD patterns collected in the experiments with the SrF-Ap material at different *P–T* conditions. All major peaks in the XRD pattern at room condition (**a**) can be attributed to the SrF-Ap structure (JCPDS 50-1744), whereas a few very weak peaks might belong to the α- and *β*-$Sr_2P_2O_7$ phases (JCPDS 24-1011 and PDF 13-0194, respectively). The XRD pattern in (**a**) is indexed for the SrF-Ap, whereas that in (**c**) is indexed for the *γ*-$Sr_3(PO_4)_2$ only (JCPDS 24-1008). In contrast, the synchrotron data (**d**; data rescaled to the wavelength of 1.54056 Å) hardly show the impurity phases and any phase transition/decomposition of the SrF-Ap

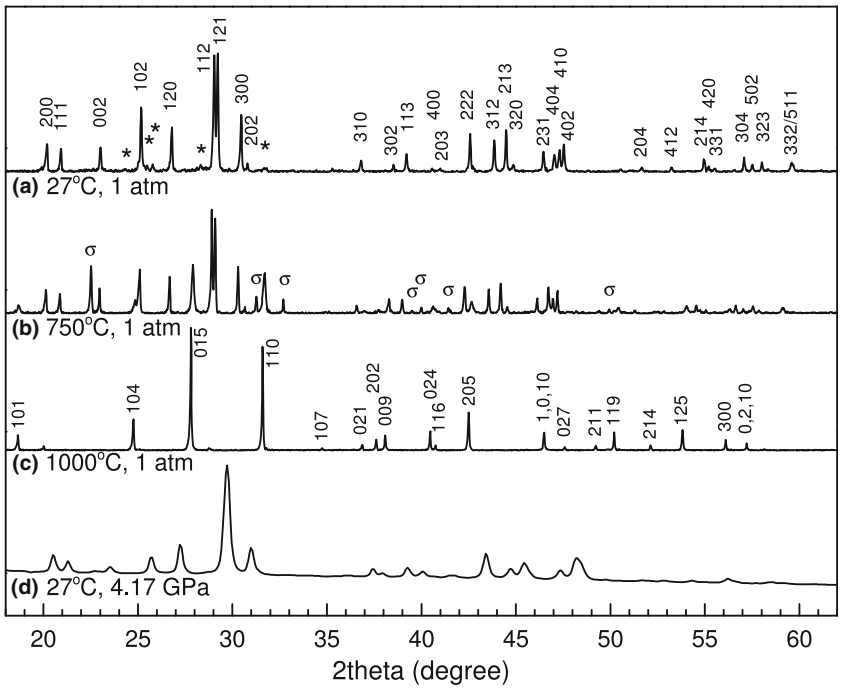


**Fig. 2** Typical XRD patterns collected in the experiments with the BaF-Ap material at different *P–T* conditions. All major peaks in the XRD pattern at room condition (**a**) can be attributed to the BaF-Ap structure (JCPDS 71-1316), whereas a few very weak peaks (denoted by the *asterisks*) belonged to some unknown phase. At temperatures between ~450 and 950 °C, the *σ*-$Ba_2P_2O_7$ phase was stable (JCPDS 30-0144). The XRD pattern in (**a**) is indexed for the BaF-Ap, whereas that in (**c**) is indexed for *γ*-$Ba_3(PO_4)_2$ only (JCPDS 25-0028). In contrast, the synchrotron data (**d**; data rescaled to the wavelength of 1.54056 Å) did not clearly show the unknown impurity phase

methanol/ethanol mixture which should secure a room-$T$ hydrostatic pressure state up to about 10 GPa (Angel et al. 2007; Klotz et al. 2009). Using the ruby fluorescence method (Mao et al. 1978), we measured the sample pressure before and after each X-ray analysis. The incident synchrotron X-ray beam was monochromatized to a wavelength of 0.4066 Å, and its beam size was collimated to a size of about 25 × 20 μm$^2$. The X-ray diffraction pattern of the sample at certain pressure was collected with an exposure time of 300 s using an online CCD detector and later integrated as a function of $2\theta$ to give the conventional one-dimensional X-ray profile using the Fit2D program (Hammersley 1996). With a full-profile refinement of the collected powder X-ray data, the positions of the diffraction peaks of the fluorapatites were determined and subsequently used to derive the unit-cell parameters at different pressures. These experimental and data-processing techniques were well established and verified in our previous studies (Liu et al. 2008; Fleet et al. 2010).

**Table 1** Unit-cell parameters of $Sr_{10}(PO_4)_6F_2$ and $Ba_{10}(PO_4)_6F_2$ at different temperatures (1 atm)

| $T$ (°C) | $a$ (Å) | $c$ (Å) | $V$ (Å$^3$) | $c/a$ |
|---|---|---|---|---|
| $Sr_{10}(PO_4)_6F_2$ | | | | |
| 27 | 9.7140(3)[a] | 7.2847(2) | 595.3(1) | 0.74991(3) |
| 50 | 9.7166(4) | 7.2864(2) | 595.8(1) | 0.74989(3) |
| 100 | 9.7225(6) | 7.2904(3) | 596.8(1) | 0.74985(6) |
| 150 | 9.7286(4) | 7.2944(2) | 597.9(1) | 0.74979(4) |
| 200 | 9.7351(6) | 7.2991(3) | 599.1(1) | 0.74977(6) |
| 250 | 9.7417(7) | 7.3039(3) | 600.3(1) | 0.74975(6) |
| 300 | 9.7481(6) | 7.3081(3) | 601.4(1) | 0.74970(6) |
| 350 | 9.7558(8) | 7.3135(4) | 602.8(1) | 0.74966(8) |
| 400 | 9.7621(6) | 7.3178(3) | 603.9(1) | 0.74961(5) |
| 450 | 9.7691(6) | 7.3229(3) | 605.2(1) | 0.74960(5) |
| 500 | 9.7762(6) | 7.3279(3) | 606.5(1) | 0.74957(6) |
| 550 | 9.7832(6) | 7.3330(3) | 607.8(1) | 0.74955(6) |
| 600 | 9.7906(7) | 7.3382(3) | 609.2(1) | 0.74952(6) |
| 650 | 9.7968(6) | 7.3431(3) | 610.4(1) | 0.74954(6) |
| 700 | 9.8021(7) | 7.3467(3) | 611.3(1) | 0.74950(6) |
| 750 | 9.8098(8) | 7.3526(4) | 612.8(1) | 0.74952(7) |
| 800 | 9.8163(13) | 7.3573(7) | 614.0(2) | 0.74950(13) |
| 850 | 9.8250(10) | 7.3629(5) | 615.5(1) | 0.74940(9) |
| 900 | 9.8322(16) | 7.3683(8) | 616.9(2) | 0.74940(15) |
| 950 | 9.8397(12) | 7.3739(6) | 618.3(2) | 0.74940(11) |
| 1000 | 9.8473(13) | 7.3791(6) | 619.7(2) | 0.74935(11) |
| $Ba_{10}(PO_4)_6F_2$ | | | | |
| 27 | 10.1612(6) | 7.7216(3) | 690.4(1) | 0.75990(6) |
| 50 | 10.1641(5) | 7.7240(2) | 691.1(1) | 0.75993(4) |
| 100 | 10.1704(7) | 7.7284(3) | 692.3(1) | 0.75990(6) |
| 150 | 10.1777(7) | 7.7342(3) | 693.8(1) | 0.75992(6) |
| 200 | 10.1852(6) | 7.7398(2) | 695.3(1) | 0.75991(5) |
| 250 | 10.1928(6) | 7.7459(3) | 696.9(1) | 0.75994(5) |
| 300 | 10.2006(6) | 7.7511(3) | 698.5(1) | 0.75987(5) |
| 350 | 10.2057(6) | 7.7563(3) | 699.6(1) | 0.76000(5) |
| 400 | 10.2136(6) | 7.7610(3) | 701.1(1) | 0.75987(5) |
| 450 | 10.2203(6) | 7.7653(3) | 702.5(1) | 0.75979(5) |
| 500 | 10.2264(6) | 7.7702(3) | 703.7(1) | 0.75982(5) |
| 550 | 10.2341(8) | 7.7748(4) | 705.2(1) | 0.75969(7) |
| 600 | 10.2385(5) | 7.7783(3) | 706.1(1) | 0.75971(4) |
| 650 | 10.2452(8) | 7.7824(4) | 707.4(1) | 0.75961(7) |
| 700 | 10.2517(5) | 7.7877(2) | 708.8(1) | 0.75965(4) |
| 750 | 10.2619(6) | 7.7918(3) | 710.6(1) | 0.75929(6) |
| 800 | 10.2682(13) | 7.7954(7) | 711.8(2) | 0.75917(12) |
| 850 | 10.2766(15) | 7.7989(7) | 713.3(2) | 0.75890(13) |

[a] Standard deviations are in parentheses

## Result and discussion

The synthesizing experiments with the SrF-Ap starting composition mainly produced the SrF-Ap, α-$Sr_2P_2O_7$ and β-$Sr_2P_2O_7$, with the SrF-Ap as the predominant phase (Fig. 1a). The electron microprobe analyses (EMPA) suggested that the composition of the SrF-Ap was $Sr_{9.5(3)}(PO_4)_6F_2$ (20 analyses), thus close to the initial design (simplified as $Sr_{10}(PO_4)_6F_2$ hereafter). In contrast, the EMPA data (10 analyses) constrained the compositions of the α-$Sr_2P_2O_7$ and β-$Sr_2P_2O_7$ phases as $Sr_{1.80(4)}P_{2.08(1)}O_7$, presumably indicating certain amount of substitution

**Table 2** Unit-cell parameters of $Sr_{10}(PO_4)_6F_2$ and $Ba_{10}(PO_4)_6F_2$ at different pressures (ambient $T$)

| $P$ (GPa)[a] | $a$ (Å) | $c$ (Å) | $V$ (Å$^3$) | $c/a$ |
|---|---|---|---|---|
| $Sr_{10}(PO_4)_6F_2$ | | | | |
| 0.0001[b] | 9.734(1)[c] | 7.302(2) | 599.2(2) | 0.7502(2) |
| 0.42(1)[d] | 9.720(1) | 7.289(1) | 596.3(1) | 0.7499(2) |
| 1.31(6) | 9.689(2) | 7.270(3) | 591.1(2) | 0.7504(3) |
| 2.51(6) | 9.643(2) | 7.246(2) | 583.5(2) | 0.7514(3) |
| 3.74(8)[d] | 9.605(1) | 7.215(2) | 576.4(2) | 0.7512(2) |
| 5.23(11) | 9.564(1) | 7.190(2) | 569.6(2) | 0.7517(2) |
| $Ba_{10}(PO_4)_6F_2$ | | | | |
| 0.0001[b] | 10.212(1) | 7.759(2) | 700.8(2) | 0.7598(2) |
| 0.69(11)[d] | 10.175(1) | 7.719(1) | 692.0(1) | 0.7586(1) |
| 1.31(1) | 10.135(1) | 7.693(1) | 684.4(1) | 0.7591(1) |
| 2.27(2) | 10.085(1) | 7.643(1) | 673.2(1) | 0.7579(1) |
| 3.03(11) | 10.044(1) | 7.596(1) | 663.6(2) | 0.7562(2) |
| 4.17(1) | 9.985(2) | 7.551(2) | 651.9(3) | 0.7563(3) |

[a] Pressure determined by averaging pressure values measured before and after collection of synchrotron data

[b] Data at ambient pressure collected on powder sample loosely packed into a small hole (400 μm across) in a stainless steel plate

[c] Standard deviations are in parentheses

[d] Data collected during decompression

between Sr and P. In addition, these compositional data of the SrF-Ap, α-$Sr_2P_2O_7$ and β-$Sr_2P_2O_7$ led to the conclusion that the starting material used in the high-*P* synthesizing experiment was enriched in P (or short in Sr), highly implying that the moisture content in the $P_2O_5$ powder was negligible. At room *P*, the phase transition *T* between the α-$Sr_2P_2O_7$ and β-$Sr_2P_2O_7$ phases is around 750 °C (Ranby et al. 1955). The coexistence of the α-$Sr_2P_2O_7$ and β-$Sr_2P_2O_7$ phases in our synthetic product thus suggests that the phase transition *T* is elevated by about 50 °C at 1.0 GPa.

The synthesizing experiments with the BaF-Ap starting composition mainly produced the BaF-Ap and an unknown phase, with the BaF-Ap as the predominant phase (Fig. 2a). The EMPA data suggested that the compositions of the BaF-Ap and unknown phase were $Ba_{9.7(1)}(PO_4)_6F_2$ (simplified as $Ba_{10}(PO_4)_6F_2$ hereafter; 15 analyses) and $Ba_{1.93(1)}P_{2.03(1)}O_7$ (10 analyses), respectively. It follows that the starting material used in synthesizing the BaF-Ap was also enriched in P (or short in Ba), but to a smaller extent in comparison with the starting material used in synthesizing the SrF-Ap. This was possibly due to the lower content of $P_2O_5$ in the ideal BaF-Ap than in the SrF-Ap.

The in situ high-*T* powder X-ray diffraction experiments were carried out up to 1,000 °C (1 atm). For the synthetic SrF-Ap material, the impurity phases coexisted with the SrF-Ap till the β-$Sr_2P_2O_7$ phase completely disappeared at ~900 °C (Fig. 1b, c). At somewhere between 850 and 900 °C, the SrF-Ap started to decompose ($Sr_{10}(PO_4)_6F_2 = 3Sr_3(PO_4)_2 + SrF_2$), with $SrF_2$ undetected by the X-ray due to its low volume proportion (Fig. 1c). The breakdown reaction, however, was not completed at 1,000 °C (Fig. 1c), and the extraction of the unit-cell parameters of the SrF-Ap from the X-ray data collected at this *T* was successful (Table 1). For the synthetic BaF-Ap material, the impurity phase disappeared at ~350 °C. At temperatures between ~450 and 950 °C, a new phase, the σ-$Ba_2P_2O_7$ phase (PDF# 30-0144), was stable. At somewhere between 650 and 700 °C, the BaF-Ap started to decompose according to the reaction $Ba_{10}(PO_4)_6F_2 = 3Ba_3(PO_4)_2 + BaF_2$, with $BaF_2$ undetected presumably due to its low volume proportion. The BaF-Ap fully decomposed at ~950 °C (Table 1), with $BaF_2$ still undetected though. With the X-ray patterns at relatively high *T* showing no peaks for any crystalline phase other than $Ba_3(PO_4)_2$ (Fig. 2), $BaF_2$ might have been dissolved into a melt phase.

The hydrostatic high-*P* experiments were conducted up to about 5 GPa (room *T*); experiments at higher pressures are not necessary since both SrF-Ap and BaF-Ap become unstable at pressures close to 5 GPa (to be reported somewhere else). No phase transition was observed for both apatites over this *P* interval. Typical powder X-ray diffraction patterns are illustrated in Fig. 1d and Fig. 2d, and the unit-cell parameters at different pressures derived from the X-ray diffraction patterns are listed in Table 2.

## Thermal expansion of SrF-Ap and BaF-Ap

Figure 3a shows the variations of the unit-cell parameters of the SrF-Ap with *T*. As *T* increases from 27 to 1,000 °C, the dimension of the *a*-axis increases by 1.35 %, that of the *c*-axis by 1.28 % and that of the volume by 3.94 %. In addition, the *c*/*a* ratio linearly decreases slightly, from 0.74991(3) to 0.74935(11) for the same *T* range (less than 0.07 %), indicating a very small variation in the thermal expansion anisotropy of the SrF-Ap (Table 1).

Figure 3b shows the variations of the unit-cell parameters of the BaF-Ap with *T*. As *T* increases from 27 to 850 °C, the dimension of the *a*-axis increases by 1.12 %, that of the *c*-axis by 0.99 % and that of the volume by 3.21 %. For the whole *T* range, the *c*/*a* ratio decreases by about 0.13 %, from 0.75990(6) to 0.75890(13), indicating a

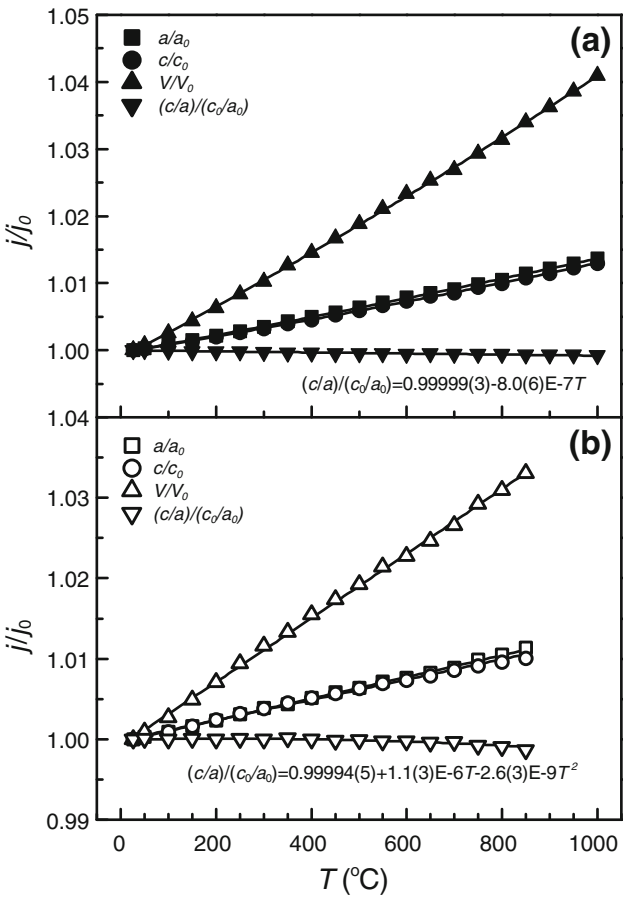


**Fig. 3** Variation of the unit-cell parameters with *T* (room *P*): **a** SrF-Ap; **b** BaF-Ap

very small variation in the thermal expansion anisotropy of the BaF-Ap (Table 1).

The $V$–$T$ data were fitted to the following equations:

$$V_T = V_0 \exp\left(\int_0^T \alpha_T \mathrm{dT}\right) \quad (1)$$

and

$$\alpha_T = a_0 + a_1 T + a_2 T^{-2} \quad (2)$$

where $V_T$, $V_0$ and $\alpha_T$ are the high-$T$ volume, room-$T$ volume and volumetric thermal expansion coefficient at temperature $T$, respectively. $a_0$, $a_1$ and $a_2$ are the constants obtained in fitting the experimental $V$–$T$ data. Replacing the volume data in the equations above with the axial dimensions, the axial thermal expansion coefficients can be obtained similarly. In the cases that $a_1$ and $a_2$ could not be resolved due to the generally narrow $T$ range in our experiments, their values are fixed as zero. For the SrF-Ap, the derived constants for the thermal expansion coefficients are $a_0 = 3.70(5) \times 10^{-5}/^{\circ}\mathrm{C}$ and $a_1 = 0.78(12) \times 10^{-8}/^{\circ}\mathrm{C}^2$ for the volume, $a_0 = 1.28(2) \times 10^{-5}/^{\circ}\mathrm{C}$ and $a_1 = 0.23(4) \times 10^{-8}/^{\circ}\mathrm{C}^2$ for the $a$-axis, and $a_0 = 1.17(2) \times 10^{-5}/^{\circ}\mathrm{C}$ and $a_1 = 0.33(4) \times 10^{-8}/^{\circ}\mathrm{C}^2$ for the $c$-axis (Table 3). For the BaF-Ap, the derived constants for the thermal expansion coefficients are $a_0 = 3.90(4) \times 10^{-5}/^{\circ}\mathrm{C}$ for the volume, $a_0 = 1.34(1) \times 10^{-5}/^{\circ}\mathrm{C}$ for the $a$-axis and $a_0 = 1.26(2) \times 10^{-5}/^{\circ}\mathrm{C}$ for the $c$-axis (Table 3).

## Compressibility of SrF-Ap and BaF-Ap

Figure 4a shows the variations of the unit-cell parameters of the SrF-Ap with $P$. For the investigated $P$ interval (1 atm to 5.2 GPa), the dimension of the $a$-axis is reduced by 1.75 %, that of the $c$-axis by 1.53 % and that of the volume by 4.94 %. In addition, the $c/a$ ratio linearly increases, from 0.7502(2) to 0.7517(2) for the same $P$ range (less than 0.20 %), indicating a small elastic anisotropy gradually reduced by $P$ for the SrF-Ap (Table 2).

Figure 4b shows the variations of the unit-cell parameters of the BaF-Ap with $P$. For the investigated $P$ interval (1 atm to 4.17 GPa), the dimension of the $a$-axis decreases by 2.22 %, that of the $c$-axis by 2.68 % and that of the volume by 6.98 %. Compared to the $c/a$ ratio of the SrF-Ap at high pressure, the $c/a$ ratio of the BaF-Ap linearly decreases, from 0.7598(2) to 0.7563(3) for the same $P$ range (less than 0.22 %), indicating a small elastic

**Table 3** Thermal expansion coefficients of various apatites (ambient $P$ and $T$)[a]

| Apatites | $j$ | $j_0$ (Å or Å$^3$)[b] | $a_0(10^{-5}/^{\circ}\mathrm{C})$ | $a_1(10^{-8}/^{\circ}\mathrm{C}^2)$ | $T$ range ($^{\circ}$C) | Reference[c] |
|---|---|---|---|---|---|---|
| $Pb_{10}(PO_4)_6F_2$ | $a$ | 9.7757(2) | 2.25(2) | –[d] | 27–600 | H11 |
| | $c$ | 7.3046(1) | 2.79(12) | – | 27–600 | H11 |
| | $V$ | 604.54(3) | 7.30(15) | – | 27–600 | H11 |
| $Ca_{10}(PO_4)_6F_2$ | $V$ | 523.6(4) | 3.40(1) | 2.90(1) | 20–907 | B99 |
| $Sr_{10}(PO_4)_6F_2$ | $a$ | 9.7140(3) | 1.28(2) | 0.23(4) | 27–1000 | This study |
| | $c$ | 7.2847(2) | 1.17(2) | 0.33(4) | 27–1000 | This study |
| | $V$ | 595.3(1) | 3.70(5) | 0.78(12) | 27–1000 | This study |
| $Ba_{10}(PO_4)_6F_2$ | $a$ | 10.161(1) | 1.34(1) | – | 27–850 | This study |
| | $c$ | 7.7216(3) | 1.26(2) | – | 27–850 | This study |
| | $V$ | 690.4(1) | 3.90(4) | – | 27–850 | This study |
| $Ca_{10}(PO_4)_6Cl_2$ | $V$ | 538.6(5) | 3.55(1) | – | 20–848 | B99 |
| $Ca_{10}(PO_4)_6(OH)_2$ | $V$ | 529.0(4) | 2.32(1) | 5.18(1) | 20–602 | B99 |
| | $V$ | 529.35(1) | 4.45(28) | – | 22–1004 | F83 |
| $Pb_{10}(P_{0.83}V_{0.17}O_4)_6F_2$ | $V$ | 607.54(3) | 7.57(8) | – | 27–600 | H11 |
| $Pb_{10}(P_{0.67}V_{0.33}O_4)_6F_2$ | $V$ | 620.5(1) | 7.72(7) | – | 27–600 | H11 |
| $Pb_{10}(P_{0.50}V_{0.50}O_4)_6F_2$ | $V$ | 633.7(2) | 7.83(8) | – | 27–600 | H11 |
| $Pb_{10}(P_{0.33}V_{0.67}O_4)_6F_2$ | $V$ | 640.2(2) | 8.19(7) | – | 27–600 | H11 |
| $Pb_{10}(P_{0.17}V_{0.83}O_4)_6F_2$ | $V$ | 651.0(3) | 8.07(17) | – | 27–600 | H11 |
| $Pb_{10}(VO_4)_6F_2$ | $V$ | 656.0(1) | 8.28(22) | – | 27–600 | H11 |

[a] Thermal expansion coefficient is defined as $\alpha = j^{-1}(\partial j/\partial T)$ in which $j$ stands for $a$, $c$ or $V$, and $T$ for temperature ($^{\circ}$C). Its relationship with $T$ is $\alpha = a_0 + a_1 T + a_2 T^{-2}$. $a_2$ is always insignificant and thus set as zero

[b] Determined by direct experimental measurement

[c] H11, He et al. (2011); B99, Brunet et al. (1999); F83, Fischer et al. (1983)

[d] Insignificant value

anisotropy gradually enhanced by $P$ for the BaF-Ap (Table 2).

In order to determine the isothermal bulk modulus, the $P$–$V$ data were fitted to the second-order Birch–Murnaghan equation of state (BM-EoS; Birch 1947) by a least-squares method, considering the narrow $P$ interval covered by our compression experiments:

$$P = 3K_T f_E(1 + 2f_E)^{\frac{5}{2}} \quad (3)$$

where $P$ is the pressure, $K_T$ the isothermal bulk modulus and $f_E$ the Eulerian definition of finite strain, which is $[(V_0/V)^{2/3}-1]/2$, respectively. In the Eulerian definition of finite strain, $V_0$ is the volume at zero pressure, whereas $V$ is the volume at high pressure. The obtained parameters are as follows: $V_0 = 599.1(1)$ Å$^3$ and $K_T = 91.1(13)$ GPa for the SrF-Ap; and $V_0 = 702.6(6)$ Å$^3$ and $K_T = 47.0(14)$ GPa for the BaF-Ap (Table 4).

A linearized second-order BM-EoS (Angel 2000) was used to obtain the parameters of the equations of state for the crystallographic axes, yielding: in the case of the SrF-Ap, $a_0 = 9.735(1)$ Å and $K_{T\text{-}a} = 86.5(15)$ GPa for the $a$-axis whereas $c_0 = 7.300(1)$ Å and $K_{T\text{-}c} = 102.2(26)$ GPa for the $c$-axis; in the case of the BaF-Ap, $a_0 = 10.213(1)$ Å and $K_{T\text{-}a} = 54.3(7)$ GPa for the $a$-axis whereas $c_0 = 7.767(3)$ Å and $K_{T\text{-}c} = 42.6(17)$ GPa for the $c$-axis (Table 4). The elastic anisotropy ($K_{T\text{-}c}$:$K_{T\text{-}a}$) of the SrF-Ap and BaF-Ap, therefore, are about 1.18(4) and 0.79(3), respectively; in other words, our two samples show generally opposite elastic anisotropies.

## Effect of the M-site cations

In the unit cell of fluorapatite (MF-Ap; $M_{10}(PO_4)_6F_2$), there are two different sites for the 10 M cations, with 4 M cations in ninefold coordination and 6 M cations in sevenfold coordination (space group $P6_3/m$; Kim et al. 2000; Hughes and Rakovan 2002; Pekov et al. 2010). Although a large number of cations can readily occupy the M sites, there are quantitative experimental data at high-$T$/$P$ conditions for the CaF-Ap, SrF-Ap, BaF-Ap and PbF-Ap only (Brunet et al. 1999; Comodi et al. 2001; Matsukage et al. 2004; Liu et al. 2008; Fleet et al. 2010; He et al. 2011, 2012). Table 5 summarizes the important properties of $Ca^{2+}$, $Sr^{2+}$, $Ba^{2+}$ and $Pb^{2+}$, which might be used to constrain the effect of the M-site cations on the thermal expansivity and compressibility of various MF-Ap. In general, ionic radius, charge and polarizability, in the order of importance, can strongly affect the physical–chemical behavior of the relevant materials; electronegativity, listed in Table 5 as well, is normally a property closely related to polarizability (Nagle 1990).

It is thus expected that the unit-cell parameters of the MF-Ap should be positively correlated with the sizes of the M cations. Fig. 5 confirms that the correlations between the sizes of the alkaline earth cations ($Ca^{2+}$, $Sr^{2+}$ and $Ba^{2+}$; ambient $P$ and $T$) and the unit-cell parameters of the MF-Ap are almost linear. In addition, the data of the PbF-Ap are plotted very close to the trends defined by the CaF-Ap, SrF-Ap and BaF-Ap. It follows that the size of the M cations is the major factor dictating the unit-cell parameters of the MF-Ap at ambient $P$–$T$ condition, with the polarizability playing a negligible role.

For the thermal expansion coefficients, vague linear correlations are demonstrated by the data of the CaF-Ap, SrF-Ap and BaF-Ap (Fig. 6), indicating the role of the size of the M cations as well. On the other hand, the thermal expansion coefficients of the PbF-Ap evidently plot off the trends defined by the CaF-Ap, SrF-Ap and BaF-Ap. Considering the similar sizes of Sr and Pb cations, this deviation hints the possible role of the very different polarizabilities of the Sr and Pb cations in dictating the thermal expansion coefficients of the MF-Ap (Table 5). Compared to the Sr–O bond, the Pb–O bond is more covalent and directional, so that it is presumably easily

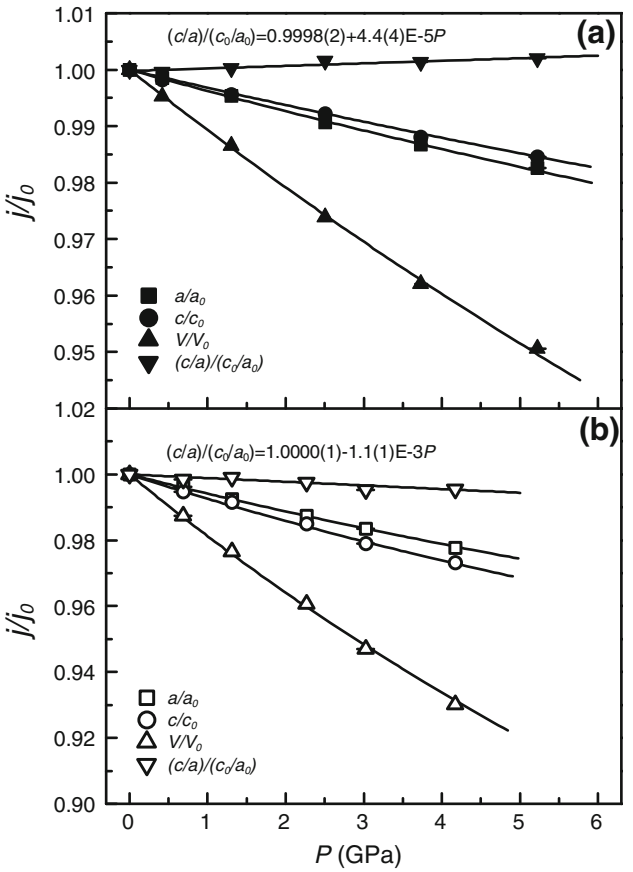


**Fig. 4** Variation of the unit-cell parameters with $P$ (room $T$): **a** SrF-Ap; **b** BaF-Ap

**Table 4** Linear and bulk moduli of various apatites (ambient $P$ and $T$)[a]

| Apatites | $V_0$ (Å$^3$)[b] | $K_T$ | $K_{T\text{-}a}$ | $K_{T\text{-}c}$ | $K_{T\text{-}c}/K_{T\text{-}a}$ | Reference[c] |
|---|---|---|---|---|---|---|
| $Ca_{10}(PO_4)_6F_2$ | 523.6(4) | 97.9(19) | – | – | – | B99 |
| | 524.2(1) | 97.8(10) | 87(3)[d] | 125(3)[d] | 1.44(6) | C01 |
| | 524.5(2) | 91.6(10) | 80(1) | 126(1) | 1.58(2) | M04 |
| $Pb_{10}(PO_4)_6F_2$ | 600.4(3) | 68.4(16) | 68(1) | 72(3) | 1.05(5) | L08 |
| $Sr_{10}(PO_4)_6F_2$ | 599.2(2) | 91.1(13) | 86.5(15) | 102.2(26) | 1.18(4) | This study |
| $Ba_{10}(PO_4)_6F_2$ | 700.8(2) | 47.0(14) | 54.3(7) | 42.6(17) | 0.79(3) | This study |
| $Ca_{10}(PO_4)_6Cl_2$ | 538.6(5) | 93.1(42) | – | – | – | B99 |
| $Ca_{10}(PO_4)_6(OH)_2$ | 529.0(4) | 97.5(18) | – | – | – | B99 |
| $Pb_{10}(P_{0.17}V_{0.83}O_4)_6F_2$ | 613.3(2) | 67.9(38) | 72(5) | 73(7) | 1.02(12) | H12 |
| $Pb_{10}(P_{0.33}V_{0.67}O_4)_6F_2$ | 620.5(1) | 57.5(50) | 59(5) | 60(6) | 1.02(13) | H12 |
| $Pb_{10}(P_{0.50}V_{0.50}O_4)_6F_2$ | 633.7(2) | 57.7(62) | 59(6) | 59(8) | 1.01(17) | H12 |
| $Pb_{10}(P_{0.67}V_{0.33}O_4)_6F_2$ | 640.2(2) | 60.2(31) | 60(3) | 71(5) | 1.19(10) | H12 |
| $Pb_{10}(P_{0.17}V_{0.83}O_4)_6F_2$ | 651.0(3) | 57.2(62) | 64(5) | 64(8) | 1.20(19) | H12 |
| $Pb_{10}(VO_4)_6F_2$ | 656.0(1) | 57.2(28) | 62(3) | 76(8) | 1.23(14) | H12 |
| LM005[e] | 527.5(1) | 84.0(10) | 73(1)[d] | 123(3)[d] | 1.69(5) | L11b |
| LM006[f] | 529.1(1) | 89.3(5) | 76(1)[d] | 131(3)[d] | 1.71(4) | L11b |

[a] The first pressure derivative of $K_T$ ($K_0$') is fixed as 4 in order to facilitate the comparison

[b] Determined by direct experimental measurement

[c] B99, Brunet et al. (1999); C01, Comodi et al. (2001); M04, Matsukage et al. (2004); L08, Liu et al. (2008); H12, He et al. (2012); L11b, Liu et al. (2011b)

[d] Obtained by recalculating the data reported in the literature with $K_0'$ fixed as 4

[e] Carbonated hydroxylapatite with the composition $Ca_{9.13}Na_{0.87}[(PO_4)_{5.05}(CO_3)_{0.95}][(OH)_{0.36}(CO_3)_{0.86}]$

[f] Carbonated hydroxylapatite with the composition $Ca_{9.66}Na_{0.35}[(PO_4)_{5.56}(CO_3)_{0.44}][(OH)_{1.45}(CO_3)_{0.33}]$

**Table 5** Comparison of ion properties of $Ca^{2+}$, $Sr^{2+}$, $Ba^{2+}$ and $Pb^{2+}$ (ambient $P$ and $T$)

| | Cation | | | |
|---|---|---|---|---|
| | $Ca^{2+}$ | $Sr^{2+}$ | $Ba^{2+}$ | $Pb^{2+}$ |
| Radius (Å): sevenfold[a] | 1.06 | 1.21 | 1.38 | 1.23 |
| Radius (Å): ninefold[a] | 1.18 | 1.31 | 1.47 | 1.35 |
| Polarizability (Å$^3$)[b] | 5.2 | 11.1 | 23.2 | 38.3 |
| Electronegativity[c] | 1.00 | 0.95 | 0.89 | 1.8 |

[a] Data from Shannon (1976)

[b] Data from Pohl (1978)

[c] Data from Ride (1998)

affected by high temperature. It is thus appropriate to claim that the polarizability of the M cations might substantially affect the thermal expansivity of the MF-Ap.

For the compressibilities, in contrast, the bulk and linear moduli of the PbF-Ap locate generally close to the trends defined by the CaF-Ap and BaF-Ap (Fig. 7), potentially indicating a negligible role of the polarizability. As the cation radius increases from Ca to Ba, interestingly, the $c$-axis of these apatites changes from less compressible to more compressible than the $a$-axis (Fig. 7d). On the other hand, the data for the SrF-Ap appear off the trends shown in Fig. 7a–c, but on the trend shown in Fig. 7d. The crystallographic details of the CaF-Ap and PbF-Ap are presently available (Hughes and Rakovan 2002; Fleet et al. 2010), whereas those of SrF-Ap and BaF-Ap are not perfect (Mathew et al. 1979; Pekov et al. 2010): The natural SrF-Ap crystal investigated by Pekov et al. (2010) contains large amounts of other components such as Ca and OH, and the BaF-Ap studied by Mathew et al. (1979) has very different positional parameters for the P, O1, O2 and O3 cations to those for the same cations in the CaF-Ap, SrF-Ap and PbF-Ap. The major differences in these four MF-Ap, considering the accuracy of the available data, include some fluctuations in the positions of the 6 M cations in sevenfold coordination and F ion. In particular, the six Sr cations in sevenfold coordination locate closer to the $c$-axis (the $y$ coordinate is 0.2393(2)), and the F ion in the SrF-Ap lies in the mirror plane (Pekov et al. 2010), suggesting strong bonding between the six Sr cations and F ion, which might result in the larger bulk and linear moduli of SrF-Ap. According to the data of the CaF-Ap and BaF-Ap (Hughes and Rakovan 2002; Mathew et al. 1979), the six Sr cations in sevenfold coordination and the F ion would be expected to shift away from, rather than closer to, the $c$-axis and from the mirror plane, respectively. More crystallographic investigations about the SrF-Ap and BaF-Ap are necessary.

## Thermal expansion and compressibility of various apatites

Figure 8 summarizes the thermal expansion coefficients (ambient $P$–$T$ condition) of various apatites ($M_{10}(BO_4)_6X_2$). It appears that there are two good positive correlations between the thermal expansion coefficients and the unit-cell volumes of the $Pb_{10}(P_{1-x}V_xO_4)_6F_2$ apatite solid solutions (He et al. 2011), and of the CaF-Ap, SrF-Ap and BaF-Ap, with the slope of the former steeper than that of the latter. The vertical shift between these two trends is potentially due to the large difference in the polarizabilities between the Pb and Ca, and Sr and Ba cations, as previously discussed. On the other hand, the difference between the slopes of these two trends possibly reflects the difference in the polarizabilities of $P^{5+}$ and $V^{5+}$ cations. The $P^{5+}$ cation in fourfold coordination (0.17 Å) is a small rigid atom with complete outermost electron shell, whereas the $V^{5+}$ cation in fourfold coordination (0.355 Å) is a relatively large soft atom with incomplete external electron shell (Shannon 1976). It is therefore expected that the polarizability of $V^{5+}$ should be significantly larger than that of $P^{5+}$, as demonstrated by the calculation done by

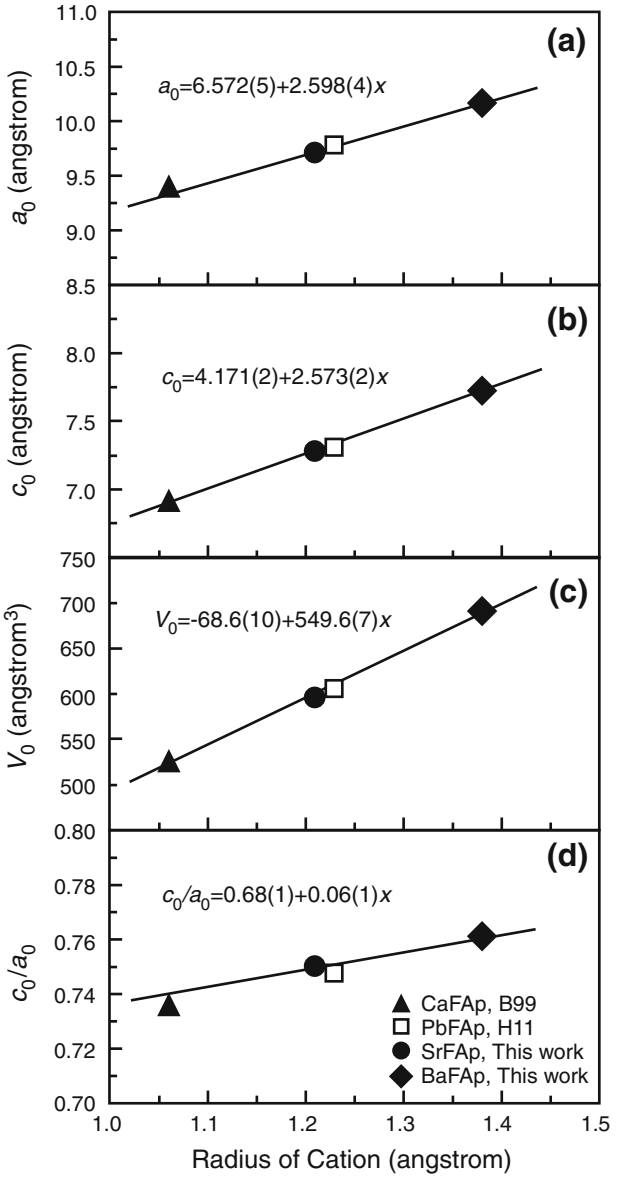


**Fig. 5** Effect of the M-site cations on the ambient $P$–$T$ unit-cell parameters of the fluorapatites $M_{10}(PO_4)_6F_2$ (M = Ca, Sr, Ba or Pb; Table 5). Data sources: CaF-Ap, B99 (Brunet et al. 1999); SrF-Ap and BaF-Ap, this study; PbF-Ap, H11 (He et al. 2011). The radii of the M-site cations in the sevenfold coordination are arbitrarily chosen. *Lines* are regressed through the CaF-Ap, SrF-Ap and BaF-Ap only

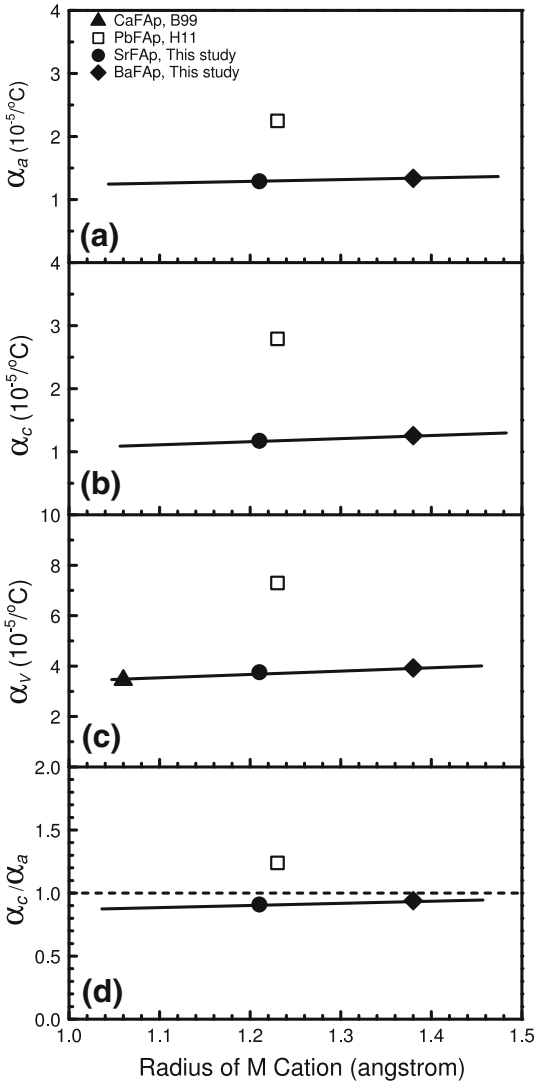


**Fig. 6** Effect of the M-site cations on the thermal expansion coefficients (ambient $T$) of the fluorapatites $M_{10}(PO_4)_6F_2$ (M = Ca, Sr, Ba or Pb; Tables 3 and 5). B99, Brunet et al. (1999); H11, He et al. (2011). The radii of the M-site cations in the sevenfold coordination are arbitrarily chosen. *Lines* are drawn through the *filled symbols* to guide the eye

Nagle (1990; 12.4 Å$^3$ for V versus 3.63 Å$^3$ for P). For the series of the solid solutions of $Pb_{10}(P_{1-x}V_xO_4)_6F_2$, the thermal expansivity of the apatites increases as $x$ increases (He et al. 2011), leading to the conclusion that larger polarizability results in larger thermal expansivity, in good agreement with the conclusion displayed by Fig. 6.

Additionally, Fig. 8 shows the effect of the X ions on the thermal expansion coefficients, with no pattern readily established though: the $Ca_{10}(PO_4)_6X_2$ (X = F, Cl or OH) apatites have much scattering thermal expansion coefficients (Fischer et al. 1983; Brunet et al. 1999).

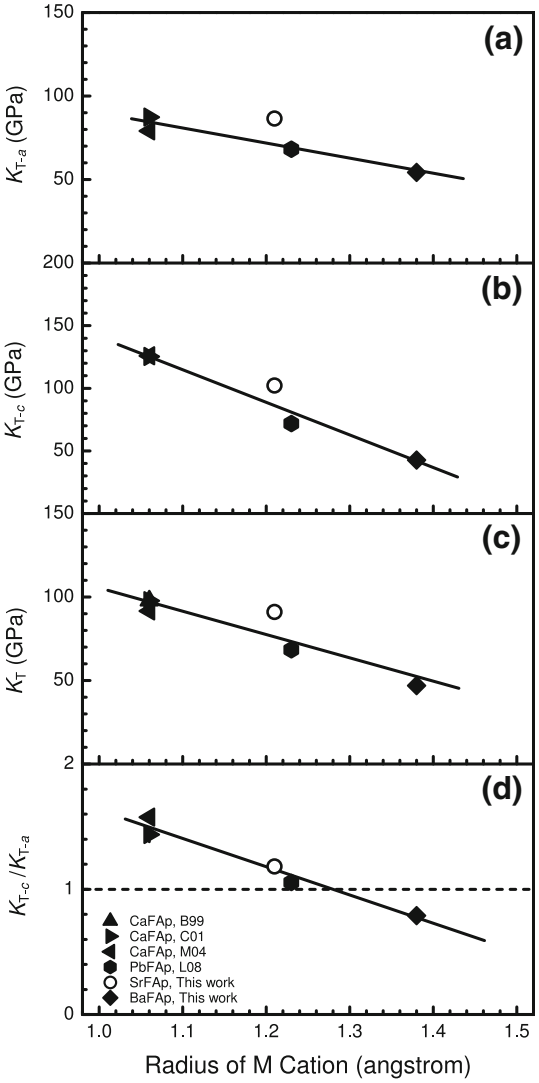


**Fig. 7** Effect of the M-site cations on the linear ($K_{T\text{-}a}$ and $K_{T\text{-}c}$) and bulk moduli ($K_T$) of the fluorapatites $M_{10}(PO_4)_6F_2$ (M = Ca, Sr, Ba or Pb; Table 4). B99, Brunet et al. (1999); C01, Comodi et al. (2001); M04, Matsukage et al. (2004); L08, Liu et al. (2008). The radii of the M-site cations in the sevenfold coordination are arbitrarily chosen. *Lines* are drawn through the *symbols* for the CaF-Ap and BaF-Ap to guide the eye. In most cases, the *error bars* are smaller than or equal to the sizes of the *symbols*

Figure 9 summarizes the bulk moduli of various apatites ($M_{10}(BO_4)_6X_2$) at ambient $P$–$T$ condition. It appears that, with the exception of the data for the SrF-Ap, all other data fall closely on a straight line:

$$K_T = 229(4) - 0.263(7) \times V_0, \quad (4)$$

where $K_T$ is in GPa and $V_0$ in Å$^3$ (the first pressure derivative of $K_T$, $K_T$', fixed as 4). With this correlation, therefore, it is possible to estimate the bulk modulus of an

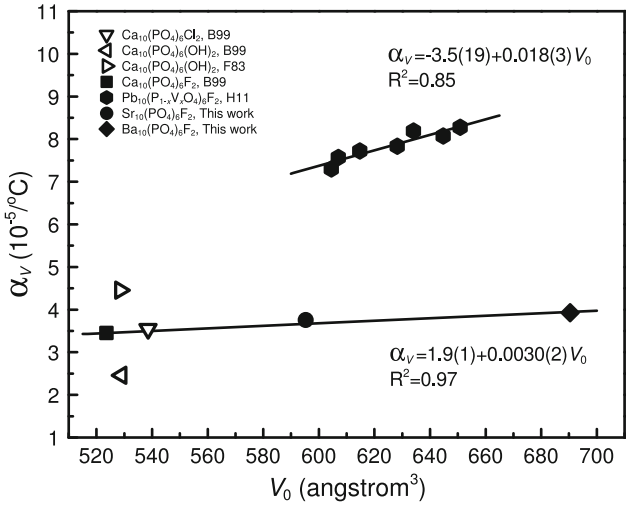


**Fig. 8** Volumetric thermal expansion coefficient (ambient $T$) versus volume of various apatites (Table 3). F83, Fischer et al. (1983); B99, Brunet et al. (1999); H11, He et al. (2011). Lines are regressed through the data points for the $Pb_{10}(P_{1-x}V_xO_4)_6F_2$ solid solutions, and the data points for the CaF-Ap, SrF-Ap and BaF-Ap only

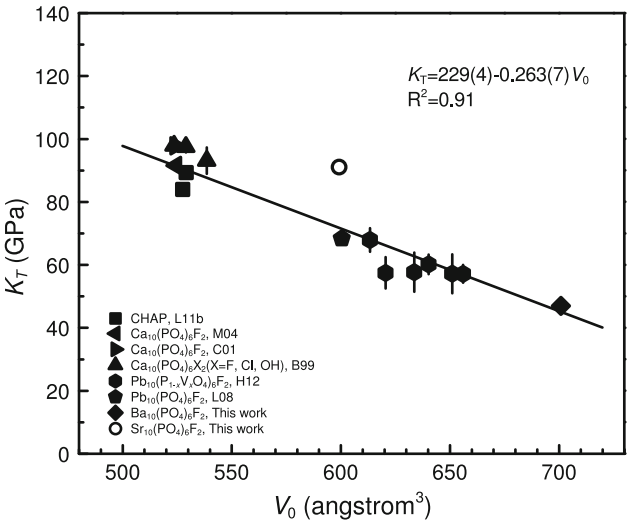


**Fig. 9** Bulk modulus versus volume of various apatites (Table 4). B99, Brunet et al. (1999); C01, Comodi et al. (2001); M04, Matsukage et al. (2004); L08, Liu et al. (2008); L11b, Liu et al. (2011b); H12, He et al. (2012). Line is regressed from all data points except that for the SrF-Ap. CHAP, carbonated hydroxylapatites (LM005 and LM006; Liu et al. 2011b)

apatite by using its volume at ambient $P$–$T$ condition. For example, the $V_0$ of the $Pb_{10}(PO_4)_6Br_2$ apatite is 646.1(1) $Å^3$, and our regressed equation estimates the $K_T$ as about 59(4) GPa, which is pretty close to the experimentally determined value (60.8(11) GPa; Liu et al. 2011a). If the data for the SrF-Ap are included in the regression, the derived equation is as follows:

$$K_T = 215(4) - 0.235 \times V_0, \quad (5)$$

and the estimated bulk modulus of the $Pb_{10}(PO_4)_6Br_2$ apatite is 63(4) GPa.

**Acknowledgments** We thank Guiming Shu and Bo Zhang for the technique support with the electron microprobe and scanning electron microscopy. We are grateful to two anonymous reviewers who provided very constructive comments to the manuscript. We thank Professor M. Matsui for his editorial handling of our paper. This investigation was financially supported by the National Natural Science Foundation of China (41090371 and 41273072) and the Key Laboratory of Earth's Deep Interior, Chinese Academy of Sciences (DQSB201101).

## References

Aissa A, Badraoui B, Thouvenot R, Debbabi M (2004) Synthesis, X-ray structural analysis and spectroscopic investigations (IR and $^{31}P$ MAS NMR) of mixed barium/strontium fluoroapatites. Eur J Inorg Chem 2004:3828–3836

Angel RJ (2000) Equation of state. In: Hazen RM, Downs RT (eds) High-temperature and high-pressure crystal chemistry. Reviews in mineralogy and geochemistry, vol 41. Mineralogical society of America, Chantilly, pp 35–60

Angel RJ, Bujak M, Zhao J, Gatta GD, Jacobsen SD (2007) Effective hydrostatic limits of pressure media for high-pressure crystallographic studies. J Appl Crystallogr 40:26–32

Birch F (1947) Finite elastic strain of cubic crystals. Phys Rev 71:809–924

Brunet F, Allan DR, Redfern SAT, Angel RJ, Miletich R, Reichmann HJ, Sergent J, Hanfland M (1999) Compressibility and thermal expansivity of synthetic apatites, $Ca_5(PO_4)_3X$ with X = OH, F and Cl. Eur J Mineral 11:1023–1035

Comodi P, Liu Y, Zanazzi PF, Montagnoli M (2001) Structural and vibrational behaviour of fluorapatite with pressure. Part I: in situ single-crystal X-ray diffraction investigation. Phys Chem Mineral 28:219–224

Edgar AD (1989) Barium- and strontium-enriched apatites in lamproites from West Kimberley, Western Australia. Am Mineral 74:889–895

Filiberto J, Treiman AH (2009) Martian magmas contained abundant chlorine, but little water. Geology 37:1087–1090

Fischer GR, Bardhan P, Geiger JE (1983) The lattice thermal expansion of hydroxyapatite. J Mater Sci Lett 2:577–578

Fleet ME, Liu X (2007) Hydrogen-carbonate ion in synthetic high-pressure apatite. Am Mineral 92:1764–1767

Fleet ME, Liu X, Shieh SR (2010) Structural change in lead fluorapatite at high pressure. Phys Chem Mineral 37:1–9

Hammersley J (1996) Fit2D report. Europe synchrotron radiation facility, Grenoble

He Q, Liu X, Hu X, Li S, Wang H (2011) Solid solution between lead fluorapatite and lead fluorvanadate apatite: mixing behavior, Raman feature and thermal expansivity. Phys Chem Mineral 38:741–752

He Q, Liu X, Hu X, Deng L, Chen Z, Li B, Fei Y (2012) Solid solutions between lead fluorapatite and lead fluorvanadate apatite: compressibility determined by using a diamond-anvil cell coupled with synchrotron X-ray diffraction. Phys Chem Mineral 39:219–226

Hu X, Liu X, He Q, Wang H, Qin S, Ren L, Wu C, Chang L (2011) Thermal expansion of andalusite and sillimanite at ambient pressure: a powder X-ray diffraction study up to 1,000°C. Min Maga 75:363–374

Hughes JM, Rakovan J (2002) The crystal structure of apatite, $Ca_5(PO_4)_3(F,OH,Cl)$. In: Kohn MJ, Rakovan J, Hughes JM (eds) Phosphates. Reviews in mineralogy and geochemistry, vol 48. Mineralogical Society of America, Chantilly, pp 1–12

Khattech I, Jemal M (1997) Thermochemistry of phosphate products. Part II: standard enthalpies of formation and mixing of calcium and strontium fluorapatites. Thermochim Acta 298:23–30

Kim JY, Fenton RR, Hunter BA, Kennedy BJ (2000) Powder diffraction studies of synthetic calcium and lead apatites. Aust J Chem 53:679–686

Klotz S, Chervin JC, Munsch P, Le Marchand G (2009) Hydrostatic limits of 11 pressure transmitting media. J Phys D Appl Phys 42:075413

Kreidler ER, Hummel FA (1970) The crystal chemistry of apatite: structure fields of fluor- and chlorapatite. Am Mineral 55: 170–184

Krenn E, Finger F (2004) Metamorphic formation of Sr-apatite and Sr-bearing monazite in a high-pressure rock from the Bohemian Massif. Am Mineral 89:1323–1329

Li Y, Zheng Y, Gong B, Fu B (2000) Carbon isotopes in eclogite and apatite separate from Huangzhen and Shima in SE Dabie. Sci China, Ser D Earth Sci 43:449–457

Liu X, Fleet ME (2009) Phase relations of nahcolite and trona at moderate P-T conditions. J Mineral Petrol Sci 104:25–36

Liu X, Shieh SR, Fleet ME, Akhmetov A (2008) High-pressure study on lead fluorapatite. Am Mineral 93:1581–1584

Liu X, Fleet ME, Shieh SR, He Q (2011a) Synthetic lead bromapatite: X-ray structure at ambient pressure and compressibility up to about 20 GPa. Phys Chem Mineral 38:397–406

Liu X, Shieh SR, Fleet ME, Zhang L, He Q (2011b) Equation of state of carbonated hydroxylapatite at ambient temperature: significance of carbonate. Am Mineral 96:74–80

Mao HK, Bell PM, Shaner JW, Steinberg DJ (1978) Specific volume measurements of Cu, Mo, Pt, and Au and calibration of rub R1 fluorescence pressure gauge for 0.006 to 1 Mbar. J Appl Phys 49:3276–3283

Mathew M, Mayer I, Dickens B, Schroeder LW (1979) Substitution in barium-fluoride apatite: the crystal structures of $Ba_{10}(PO_4)_6F_2$, $Ba_6La_2Na_2(PO_4)_6F_2$ and $Ba_4Nd_3Na_3(PO_4)_6F_2$. J Solid State Chem 28:79–95

Matsukage KN, Ono S, Kawamoto T, Kikegawa T (2004) The compressibility of a natural apatite. Phys Chem Mineral 31:580–584

Moëlo Y, Rouer O, Bouhnik-Le Coz M (2008) From diagenesis to hydrothermal recrystallization: polygenic Sr-rich fluorapatite from the oolitic ironstone of Saint-Aubin-des-Châteaux (Armorican Massif, France). Eur J Mineral 20:205–216

Murayama JK, Nakai S, Kato M, Kumazawa M (1986) A dense polymorph of $Ca_3(PO_4)_2$: a high pressure phase of apatite decomposition and its geochemical significance. Phys Earth Planet Inter 44:293–303

Nagle JK (1990) Atomic polarizability and electronegativity. J Am Chem Soc 112:4741–4747

Pan Y, Fleet ME (2002) Compositions of the apatite-group minerals: substitution mechanisms and controlling factors. In: Kohn MJ, Rakovan J, Hughes JM (eds) Phosphates. Reviews in Mineralogy and Geochemistry, vol 48. Mineralogical Society of America, Chantilly, Virginia, pp 13–49

Pekov IV, Britvin SN, Zubkova NV, Pushcharovsky DYu, Pasero M, Merlino S (2010) Stronadelphite, $Sr_5(PO_4)_3F$, a new apatite-group mineral. Eur J Mineral 22:869–874

Pohl D (1978) Electronic polarizabilities of ions in doubly refracting crystals. Acta Crystallogr A34:574–578

Ranby PW, Mash DH, Henderson ST (1955) The investigation of new phosphors, with particular reference to the pyrophosphates. Br J Appl Phys 6:S18

Ride DR (1998) Handbook of chemistry and physics (79th edition). CRC Press, Boca Raton

Sghir B, Hlil EK, Laghzizil A, Boujrhal FZ, Cherkaoui El Moursli R, Fruchart D (2009) Structure electronic and ionic conductivity study versus Ca content in $Ca_{10-x}Sr_x(PO_4)_6F_2$ apatites. Mater Res Bull 44:1592–1595

Shannon RD (1976) Revised effective ionic radii and systematic studies of interatomic distances in halides and chalcogenides. Acta Crystallogr A32:751–767

Solovova IP, Girnis AV, Ryabchikov ID, Kononkova NN (2009) Mechanisms of formation of barium-rich phlogopite and strontium-rich apatite during the final stages of alkaline magma evolution. Geochem Int 47:578–591

Zhang W, Shao J, Wang R, Xu X, Che X, Yang Y (2011) Sr-rich apatite from the Dangzishan leucitite-ijolite xenoliths (Heilongjiang Province): mineralogy and mantle-fluid metasomatism. Chin Sci Bull 56:53–63